

ER-2 Doppler Radar Investigations of the Eyewall of Hurricane Bonnie during the Convection and Moisture Experiment-3

GERALD M. HEYMSFIELD

NASA Goddard Space Flight Center, Greenbelt, Maryland

JEFFREY B. HALVERSON

Joint Center for Earth Systems Technology, University of Maryland, Baltimore County, Baltimore, Maryland

JOANNE SIMPSON

NASA Goddard Space Flight Center, Greenbelt, Maryland

LIN TIAN

Universities Space Research Associates, Seabrook, and Goddard Earth Science and Technology Center, University of Maryland, Baltimore County, Baltimore, Maryland

T. PAUL BUI

NASA Ames Research Center, Moffet Field, California

(Manuscript received 23 August 2000, in final form 10 April 2001)

ABSTRACT

A persistent, mesoscale region of intense eyewall convection contained within Hurricane Bonnie on 23 August 1998 is examined from multiple observations synthesized from the National Aeronautics and Space Administration ER-2 and DC-8 aircraft. The intense convection occurred late in the day as Bonnie was attaining its minimum central pressure and during a stage when the inner core featured a markedly asymmetric structure. The internal structure of this convective burst and its relationship to the warm core are presented using a synthesis of high-resolution satellite, aircraft radar, and in situ data. An exceptionally vigorous eyewall tower within the burst and penetrating to nearly 18 km is described. A second intense eyewall tower, adjacent to the eye, is shown to be associated with a mesoscale subsiding current of air, with vertical velocities on the order of several meters per second that descends at least 9 km and extends horizontally nearly 25 km into the eye interior. The subsidence is a much deeper and broader-scale feature than the convectively induced, symmetric overturning that commonly occurs on the upper-level flanks of convective towers in other tropical environments. The air supplying the deep current probably originates both at tropopause height and also from air detrained out of the adjacent updraft at midlevels. Strong downdrafts within the eye could not be associated with every hot tower. Whether this result was due to undersampling by aircraft or whether deep eye downdrafts are indeed sporadic, it is plausible that up to 3°C of midlevel eye warming observed in Bonnie may arise from one or more of these convectively induced episodes rather than as a result of a gradual sinking motion applied uniformly throughout the eye.

1. Introduction

Factors leading to changes in hurricane intensity, especially at landfall, are of vital importance. Intensity forecasts have little skill and have shown only slight improvement in the past 20 yr (DeMaria and Kaplan 1999). Several factors have been identified that contribute to intensification, such as warmer sea surface

temperatures and dynamically forced strengthening of the upper-level outflow (Riehl 1954). Gray (1998) has hypothesized that sudden penetration of convergent wind surges near the surface leads to unusually intense convection (extreme convection) from inflow of high-equivalent-potential-temperature (θ_E) air. This high-energy air is carried aloft by giant cumulonimbus "hot towers" (Malkus and Riehl 1960) leading to warming of the inner core. It is in light of these hot towers that we examine an example of intense, long-lived ensembles of deep convection, often referred to as "convective bursts," within the eyewall of tropical cyclone Bonnie.

Corresponding author address: Gerald M. Heymsfield, NASA/GSFC, Code 912, Greenbelt, MD 20771.
E-mail: heymsfield@agnes.gsfc.nasa.gov

Several case studies spanning nearly thirty years, pioneered by Gentry et al. (1970) and more recently by Holliday and Thompson (1979), Steranka et al. (1986), Zehr (1992), Lyons and Keene (1994), and Rodgers et al. (1998), point toward a relationship between the occurrence of convective bursts and sudden intensification. In this paper, a convective burst is defined as a group or succession of hot towers topped by an anomalously cold anvil cloud mass (seen in geostationary IR imagery) covering an area larger than the meso- γ scale. The anvil rapidly expands with time, remaining stationary relative to the center location for several hours. Some of the deep cumulonimbi or hot towers may be exceptionally vigorous and may overshoot their equilibrium level.

In addition, recent hurricane intensity change studies have focused on warm-core anomalies observed in microwave satellite observations (Kidder et al. 1978; Velden et al. 1991). A recent study utilizing data from the Advanced Microwave Sounding Unit (AMSU) on National Oceanic and Atmospheric Administration satellite *NOAA-15* (Velden et al. 1999) confirmed that significant warming occurred through deep layers in the eyes of hurricane Georges and Bonnie during 1998. This latter work provides a link between the magnitude of the satellite-derived warm core and the surface pressure at the storm center, assuming the storm was in hydrostatic balance. What has not been understood well, however, is the details of the mechanisms producing these warm cores. This important and controversial issue has been addressed with models (Smith 1980; Zhang et al. 2000) and observations (Malkus 1958; Kuo 1959; Shapiro and Willoughby 1982; Willoughby 1998). Many of the proposed mechanisms linking core warming with deepening of the storm invoke an important role for subsidence in the eye. In most convective burst studies, information on burst morphology and the relationship to the warm core was obtained from passive remote sensors. In this paper, we provide detailed observations on the internal three-dimensional structure of a convective burst, including examples of vigorous hot towers and the convective-scale air motions contained within them.

Unique to this study is observational evidence for a broad current of strong (several meters per second) descent induced at the tropopause on the flank of an intense hot tower. The current penetrated 9–10 km downward and 20–25 km outward into the eye. Observations of strong convective downdrafts along the outer edge of the eye have been described by Marks et al. (1992), who found small regions of descent as large as 5 m s^{-1} in midlevels of the storm. Another observation of strong descent inside the eye induced by intense convection was discussed by Stossmeister and Barnes (1992), but they inferred the presence of deep, mesoscale descent based on properties of downdraft air sampled in the subcloud layer. There have been few in situ observations of stratospheric penetration of convective towers. Danielsen (1993) found from ER-2 in situ measurements above 16 km in Cyclone Cecil that the tropopause was domed

above the cyclone in the form of a cirrus umbrella, but there were no appreciable convective overshoots.

During the 1998 hurricane season, the National Aeronautics and Space Administration (NASA) conducted the Convection and Moisture Experiment-3 (CAMEX-3, <http://ghrc.msfc.nasa.gov/camex3>) in conjunction with the NOAA annual campaign of hurricane observations. These two programs worked toward common goals of the U.S. Weather Research Program. CAMEX-3 focused on hurricane objectives, including synoptic flow and inner-core dynamics. The NASA ER-2 and DC-8 participated with three NOAA aircraft (WP-3D Orion aircraft Nos. *NOAA-42* and *NOAA-43* and the Gulfstream G-IVSP aircraft) on a comprehensive study of Hurricane Bonnie on 23 August 1998. The mission goals for 23 August were to discern eyewall structure of a moderate, nearly stationary hurricane, and to provide improved initial conditions for track models.¹ A variety of remote sensing instruments, including radars, microwave visible-to-infrared-range radiometers, and lidar were flown on the ER-2 and DC-8. In addition, the DC-8 carried in situ sensors for meteorological parameters and microphysics measurements. A study of Hurricane Georges with these CAMEX-3 aircraft documented the effects of the Dominican Republic's mountains on the hurricane (Geerts et al. 2000).

The NASA ER-2 aircraft was instrumented with the ER-2 Doppler Radar (EDOP), which is an X-band (9.6 GHz) Doppler radar with dual 3° beamwidth antennas fixed at nadir and 30° forward of nadir (Heymsfield et al. 1996). Datasets from EDOP will be a principal focus in this paper, corroborated by in situ flight-level measurements and dropsondes deployed within the eye and in the environment of intense convection. In section 2 of this paper, we present a concise description of the various observational platforms utilized throughout the study. In section 3, the morphology of the convective burst associated with the subsidence is discussed in terms of its larger-scale, dynamic evolution as viewed from satellite. In section 4, the finescale structure of hot towers and subsident region contained within the convective burst is presented from the vantage of the EDOP. These findings are summarized in section 5, along with discussion of possible mechanisms leading to broad-scale sinking motion in the eye region and its importance in the formation of Bonnie's warm anomaly.

2. Data and methods

a. EDOP processing and analysis

Details of the EDOP instrument may be found in Heymsfield et al. (1996). During the 23 August 1998 Bonnie flight, data were collected on the EDOP nadir beam with a 37.5-m gate spacing, and a pulse-repetition

¹ Mission summary for flight 980823H, obtained from NOAA Hurricane Research Division (HRD).

frequency of 4400 Hz providing a Nyquist velocity of about 34 m s^{-1} . Processed reflectivities and Doppler velocity were obtained every 0.5 s, which corresponds to approximately 100 m of aircraft translation (aircraft ground speed is about $200\text{--}220 \text{ m s}^{-1}$). This rate oversamples precipitation but is performed to maximize resolution near cloud top and to allow for better aircraft motion corrections. The reflectivity data have been calibrated to within about 1 dBZ. These reflectivities are corrected for attenuation using the surface reference approach (Iguchi and Meneghini 1994). The accuracy of this correction was slightly compromised because EDOP's nadir "surface" channel was not available and the surface return saturated the receiver in some of the lighter rain (weaker attenuation) periods. The mean Doppler velocity measurements have a standard deviation of about 0.1 m s^{-1} for typical rain situations and excluding aircraft motions, which can produce significantly larger uncertainties.

Calculation of vertical air motions w from the EDOP-measured Doppler velocities have been described in Heymsfield et al. (1999). A number of steps are involved in going from the measured nadir-beam Doppler velocities v_D to gridded vertical velocity fields. Aircraft motions are first removed from the v_D using flight parameters from the ER-2 inertial navigation system and the antenna tilt angles (the nadir antenna is not exactly pointed at nadir). The Doppler velocities with aircraft motion removed are vertical hydrometeor motions v_h from which the vertical air motion $w = v_h + v_i$ can be obtained with a hydrometeor fall speed v_i assumption based on the reflectivity. The v_h and reflectivity measurements are interpolated to two-dimensional grids with identical sampling as the nadir measurements (100 m horizontal, 37.5 m vertical) to correct for pitch variations of the aircraft. Minor filtering of the grids was performed both horizontally and vertically.

Calculation of w requires estimation of the v_i at each grid point. The v_i estimation is the most critical assumption in obtaining w , because v_i depends on many factors such as particle phase, size distributions, and so on. The approach is similar to that used by Marks and Houze (1987) and Black et al. (1996), which uses reflectivity- v_i relations for the snow, rain, transition (melting), and convective regions. Stratiform regions are separated vertically into three regions: rain, snow, and transition region corresponding to the melting layer. Their approach was modified slightly for EDOP observations by using a more realistic rain reflectivity- v_i relation derived for a gamma distribution, and also a parabolic profile is assumed in the transition region instead of a linear profile (Heymsfield et al. 1999). Details of the partitioning are described in the aforementioned papers. Difficulties in fall speed estimation occur in mixed-phase regions associated with convection where strong updrafts can loft liquid water, frozen rain, and graupel several kilometres above the melting level. Fall speeds for graupel are usually between those of snow and rain,

but hail or high-density ice of several millimeters can exceed fall speeds of rain; EDOP observations from a midlatitude wintertime squall line had small hail with fall speeds in excess of 10 m s^{-1} (Heymsfield et al. 1999). Black and Hallett (1986) documented hurricane microphysics with the WP-3D aircraft and found that convection was almost completely glaciated above the -5°C level and that millimeter-diameter graupel was common. Thus, w estimates can be subject to errors of several meters per second in convective regions as a result of improper fall speed estimates.

b. In situ meteorological parameters

The DC-8 in situ measurements were composed of standard flight-level measurements using the Data Acquisition and Distribution System (DADS), plus several special, higher-accuracy humidity and wind measuring systems. DADS records the aircraft navigational information and various meteorological parameters, but the accuracies were unknown because these are operational measurements; therefore, humidity and wind measurements do not use DADS data. Four separate instruments provided humidity measurements, but this study uses data only from the Jet Propulsion Laboratory laser hygrometer, which has high accuracy in a range of moisture conditions (May 1998). This instrument is based upon a near-infrared tunable diode laser source operating near $1.37 \mu\text{m}$. Originally designed for stratospheric measurements, its precision is 0.05 ppmv (parts per million by volume) in the stratosphere and also is very accurate at lower altitudes. This instrument is unaffected by wetting as with other humidity sensors. The temperature, pressure, and humidity measurements were used to calculate θ_E using the method described by Bolton (1980). The Meteorological Measurement System (MMS) on the DC-8 (Chan et al. 1998) provided high-accuracy 5-Hz wind measurements in addition to independent temperature and pressure measurements. Accuracies of the MMS are $\pm 0.3 \text{ hPa}$ for pressure, $\pm 0.3^\circ\text{C}$ for temperature, $\pm 1 \text{ m s}^{-1}$ for horizontal wind vector, and $< 1 \text{ m s}^{-1}$ for vertical wind vector.

3. Evolution of the convective burst: Mesoscale structure

a. Satellite IR evolution

The initial intensification of Bonnie from tropical depression to hurricane status commenced late in the day on 20 August 1998 (Fig. 1). Hurricane Bonnie first developed an eye early on 22 August, with the deepening trend continuing until a surface minimum pressure of 954 hPa was reached near 0000 UTC 24 August. During the intensification period, convective bursts were noted in both the satellite IR observations and also by the NASA aircraft pilots. An initial burst formed adjacent to the evolving eye late on 21 August. Its hot towers,

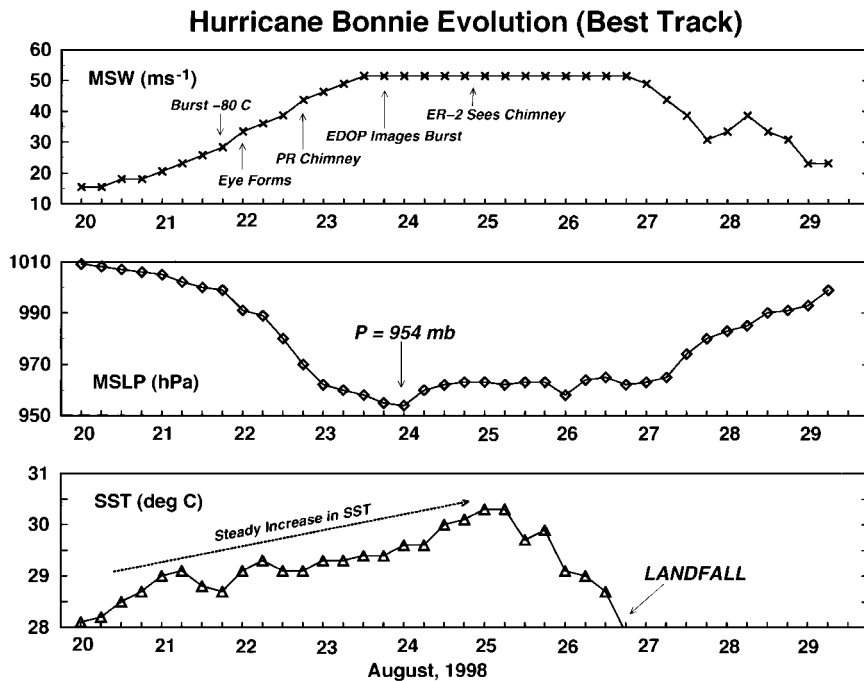


FIG. 1. Time history of Hurricane Bonnie. Shown are mean surface winds (MSW), mean sea level pressure (MSLP), and sea surface temperatures (SST). See text for details.

observed during the aircraft mission, were overshooting the tropopause by about 2 km based on soundings from Puerto Rico, which consistently had a sharp tropopause at 15.3 km, and the EDOP reflectivity measurements presented later in Figs. 6, 7, 9, and 10. Within 6 h of this burst, a closed eye appeared in the satellite imagery. In addition, on 22 August, the Tropical Rainfall Measuring Mission precipitation radar observed an exceedingly tall hot tower, or "chimney" cloud, in the inner eyewall that topped 18 km. The maximum surface winds of about 52 m s^{-1} were reached and maintained after these episodes of intense convective activity and near the time of the minimum surface pressure (0000 UTC 24 August). Bonnie moved toward the northwest from 21 August to late on 23 August, at which time its motion slowed and it took a more north-northwesterly direction until 26 August.

The intensification of Bonnie is shown in Fig. 2 with a larger-scale sequence of Geostationary Operational Environmental Satellite (GOES) IR satellite imagery from 1645 UTC 23 August (Fig. 2a) to 0215 UTC 24 August (Fig. 2f). The approximate position of the circulation center based on "best track" is marked on the images. The coldest IR temperatures, with brightness temperature T_b less than 200 K, are depicted by white regions embedded in the overall cloud shield (mostly red colors) and define the mesoscale extent of the burst in the inner-core region. This sequence indicates a strongly asymmetric region of coldest cloud-top temperatures undergoing a pronounced expansion between 1915 and 0015, with the most active convection concentrated in the

northeast quadrant of Bonnie. The asymmetric mesoscale burst in the inner eyewall (most evident at 0115 UTC 24 August, when the cold cloud shield was about 75 km in diameter) persists for about 10 h in the same location relative to the center of the vortex.

Persistent formation of intense convective cells in the same quadrant of the eyewall is often observed in tropical cyclones (Simpson 1966; Gentry 1970). In the case of Bonnie, this may have been caused by speed convergence established by a low-level jet identified in the WP-3D aircraft NOAA-42 flight-level wind analysis. Objective analysis of WP-3D flight-level winds, based on multiple transects across the storm at roughly 4 km, revealed a small region of $>40 \text{ m s}^{-1}$ airflow embedded within the more uniform 35 m s^{-1} eyewall current in the southeast quadrant. The area of speed convergence downwind of the wind maximum coincides with persistent, new cell growth on the upwind edge of the convective burst. Furthermore, as Fig. 1c shows, the sea surface temperature (SST) was steadily increasing during the period of Bonnie's intensification—potentially increasing the instability of inflow air and contributing to the vigor of the convective burst that developed late on 23 August.

Focusing on the finer-scale structure of this burst reveals considerable evolution within the coldest IR temperature region (Fig. 3). The evolution of these temperatures is shown in Fig. 3 for a period covering the aircraft flights (1846 to 2145 UTC). During this sequence, GOES was in a short-interval mode, and images were collected at approximately 7.5-min intervals. The

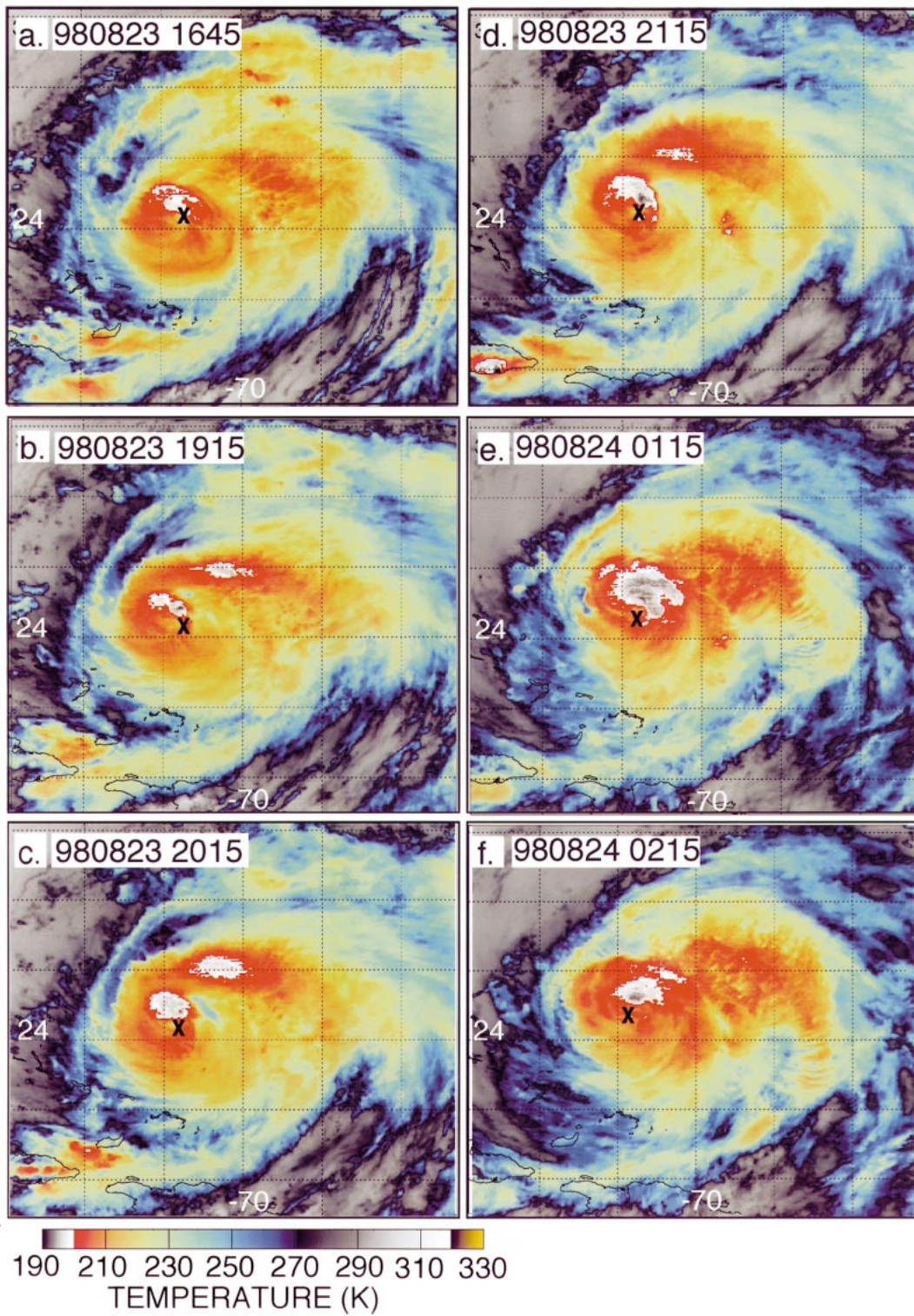


FIG. 2. Sequence of GOES IR images from Hurricane Bonnie covering late 23–early 24 Aug 1998. Color enhancement of the images highlights the cold cloud tops associated with Bonnie. Grid lines are in 2° intervals. An "x" marks the approximate position of the circulation center.

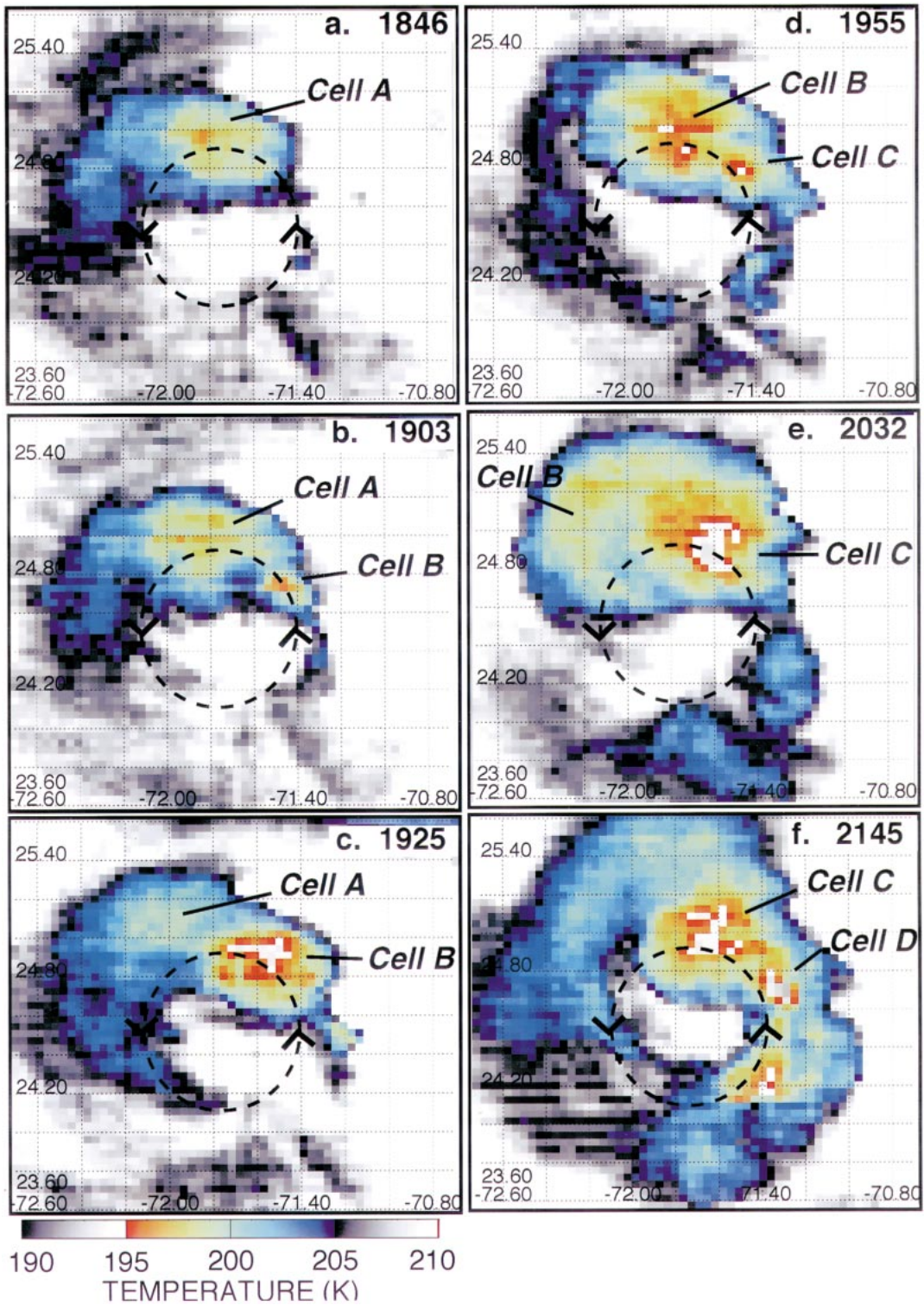


FIG. 3. Sequence of zoomed IR images covering period of ER-2 flights on 23 Aug 1998. The color table highlights the cold overshooting cloud tops and the cirrus outflow from them. The dashed circular region of about 70 km in diameter provides the approximate eyewall location. Cells are labeled A–D. Grid lines are in 0.2° intervals.

inner-core region and approximate inner-eyewall location is about 70 km in diameter based on the eyewalls observed in EDOP vertical reflectivity sections such as presented later in Figs. 6 and 9. This region is represented by a 70-km circle on the images in Fig. 3, assuming no change in diameter over the 3-h period. The hurricane motion during the sequence is toward the west-northwest. Convective activity is vigorous throughout the burst lifetime, and the deepest hot towers associated with coldest temperatures are east and north of the circulation center in the northeast quadrant. Several hot towers labeled cells A, B, C, and D persist for 30 min or more, with minimum temperatures of 190–195 K, and are presumed to be associated with overshooting convection along the northeast eyewall of Bonnie. The cells develop in succession near the same genesis region before 2100 UTC, then weaken, and finally advect cyclonically and outward from the eyewall. After 2100, convective activity began to propagate southward along the eastern eyewall. Of particular interest is the fact that a portion of the cirrus outflow from the vigorous cells advects over the northeast quadrant of the eye, causing it to be obscured by a cirrostratus layer. This cirrostratus is very significant because ice hydrometeors originating from it act as radar tracers for a deep subsidence region in the eye as described in more detail in section 4a. It is noteworthy that the eyewall is partially open until about 2145 23 August (Fig. 3f), which is also evident in the radar reflectivities presented later in section 3.2.

b. Relationship between upper-level warm anomaly, winds, IR temperatures, and low-level radar reflectivity

The warm anomaly has long been linked to hurricane intensity (e.g., Malkus and Riehl 1960; Hawkins and Rubsam 1968). To facilitate discussion of EDOP observations of the eyewall and convective burst structure in Bonnie, two-dimensional maps of in situ measurements were constructed from the DC-8 flight-level data. The DC-8 flew multiple passes across Bonnie at 11.75 ± 0.2 km altitude over an approximately 2.8-h period, thereby allowing for construction of a two-dimensional map of thermodynamic parameters and winds under a quasi-steady state assumption (Fig. 4). Figures 4a,b and 4c,d correspond, respectively, to two EDOP flight lines beginning at about 1950 and 2115, described in detail in section 4. Figure 4a shows two-dimensional maps of θ_E , MMS-derived horizontal wind, GOES IR brightness temperature at 1955 UTC enhanced for cold cloud tops, updrafts greater than 3 m s^{-1} , downdrafts less than -2 m s^{-1} , and DC-8 dropsonde release locations. The quantity θ_E is conserved and has been widely used for studying hurricane warm cores (Malkus and Riehl 1960; Simpson et al. 1998). Figure 4b shows a composite radar image from the NOAA-42 C-band lower fuselage radar at 1950. Figures 4c,d are similar to Figs.

4a,b, except they focus on the second period near 2115, and the mixing ratio is plotted in Fig. 4c, instead of θ_E . Mapping of θ_E , winds, and mixing ratio (Figs. 4a,c) was performed by computer contouring of the irregularly spaced data points along each of the DC-8 passes across Bonnie. These passes were at nearly constant altitude and, because Bonnie's motion was slow during 23 August, a correction for hurricane translation was not performed. Evident at both times are an asymmetric eyewall, with most of the heavy rain on the east side of the eye (Figs. 4b,d), and a complete absence of an eyewall in the northwest and southwest quadrants.

Figure 5 shows skew T plots and height profiles of θ_E from 4 of the 10 dropsonde releases and fall trajectories from the DC-8. The locations of these dropsonde releases are shown in Figs. 4a,c, except for the 1944 release, which is 250 km east of the circulation center. The release at 1859 (Fig. 4a) passes along the inner edge of the south eyewall, the 2126 release (Fig. 4b) passes approximately down the center of the eye, the 1944 release (Fig. 4c) represents the environment east of the circulation, and the 2040 release (Fig. 4d) represents the close-in northwest hurricane environment. The global positioning system measurements failed for three of the dropsondes (1859, 2126, and 1944 UTC), and thus no horizontal winds were available. Accuracies of the sondes are ± 0.5 hPa for pressure, $\pm 0.2^\circ\text{C}$ for temperature, and $\pm 0.5 \text{ m s}^{-1}$ for horizontal wind vector (Hock and Franklin 1999). Sonde data were not available during the first 1 km of fall from the aircraft, so the θ_E profile is extended to the DC-8 level using the flight-level value. These sondes will be referred to later in this section and in section 5.

The θ_E contours (Fig. 4a) indicate a well-defined warm core with a 368-K maximum, implying a 10–12-K perturbation from the ~ 356 – 358 -K environmental values outside of the inner-core region (Fig. 5c and the farther-out DC-8 in situ θ_E show the ambient values). The inner eyewall location is evident by the ring of vertical motions denoted by “+” in Fig. 4a, and this roughly coincides with the 362-to 364-K contours in θ_E . The mixing ratio indicates drier air north of the circulation center and moister air south and southwest of the center, although the actual values are very small at the near-12-km altitude. This moisture pattern is unexpected in view of the colder IR temperatures. It will be seen later in this section that the DC-8 is detecting subsidence and drying (i.e. layers “S₁,” “S₂,” and “S₃” in Fig. 5b) below a cirrostratus outflow layer.

The superposition of GOES IR temperatures and low-level radar reflectivity depicts a highly tilted, spiral conveyor belt of moisture within the convective burst. The low-level hurricane inflow is located along the southeast quadrant of the circulation. This air ascends rapidly and wraps cyclonically toward the northeast quadrant in intense eyewall convection and exits at upper levels as cold cirrus outflow of the convective burst (in the northwest quadrant relative to the center of the

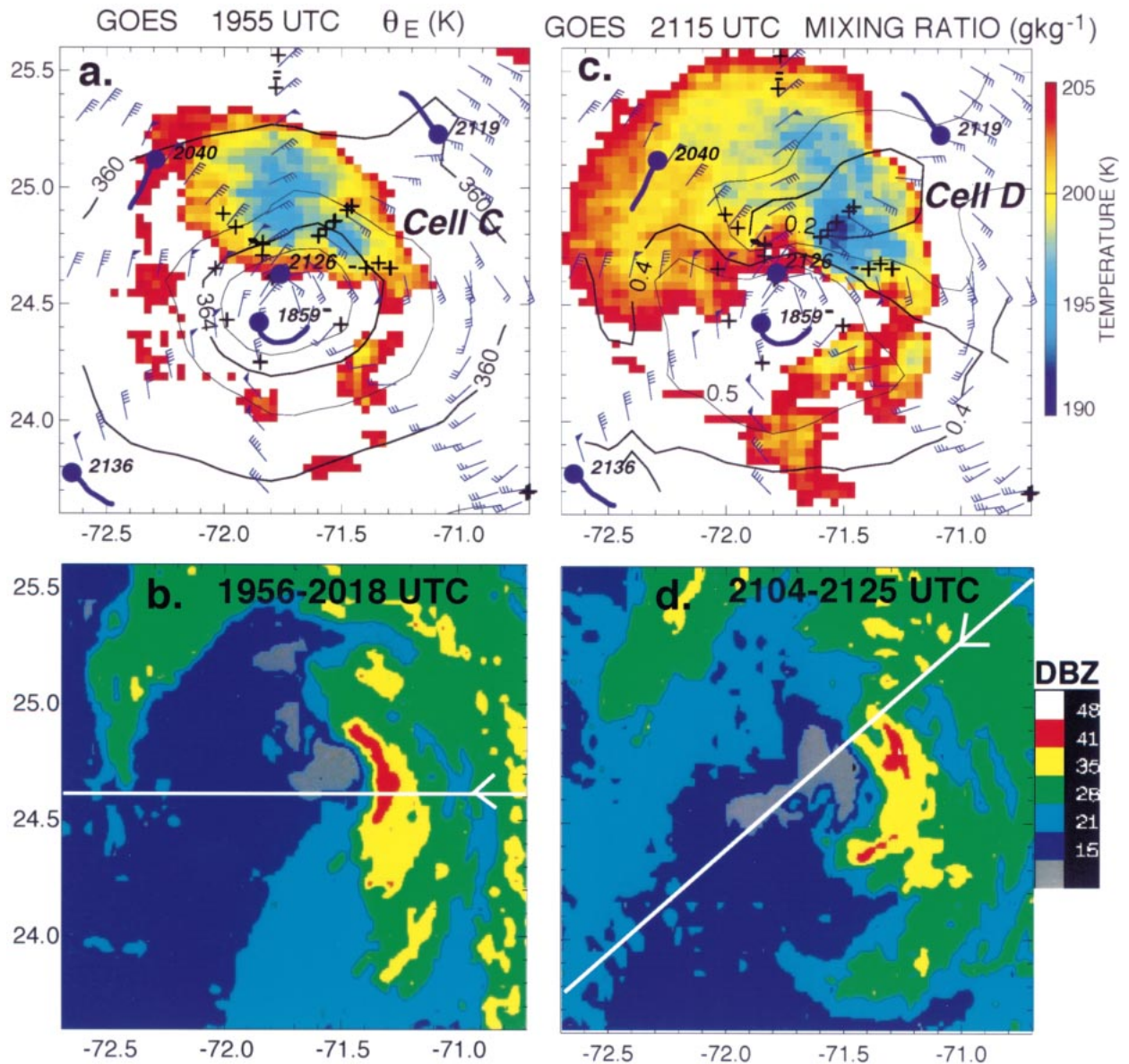


FIG. 4. Flight-level analyses at approximately 11.8-km altitude derived from DC-8 in situ measurements during 1850–2136 UTC 23 Aug 1998: (a) θ_E in 2-K intervals; wind barbs (pennant: 25 m s^{-1} ; flag: 5 m s^{-1} ; half flag: 2.5 m s^{-1}); vertical motions exceeding $|3 \text{ m s}^{-1}|$ denoted with “+” and “-”, respectively; 1955 GOES IR temperatures less than 210 K; dropsonde locations and fall trajectories; (b) the WP-3D NOAA-42 lower-fuselage composite radar echo at about 1900 and the ER-2 flight track near this time; (c) mixing ratio instead of θ_E in 0.1 g kg^{-1} intervals and the 2115 GOES IR temperatures; (d) the composite radar image at about 2100. See text for details.

circulation). Furthermore, the DC-8 in situ winds are strongest outside of the western and southwestern eyewall, suggesting upward vertical transfer of momentum in this region.

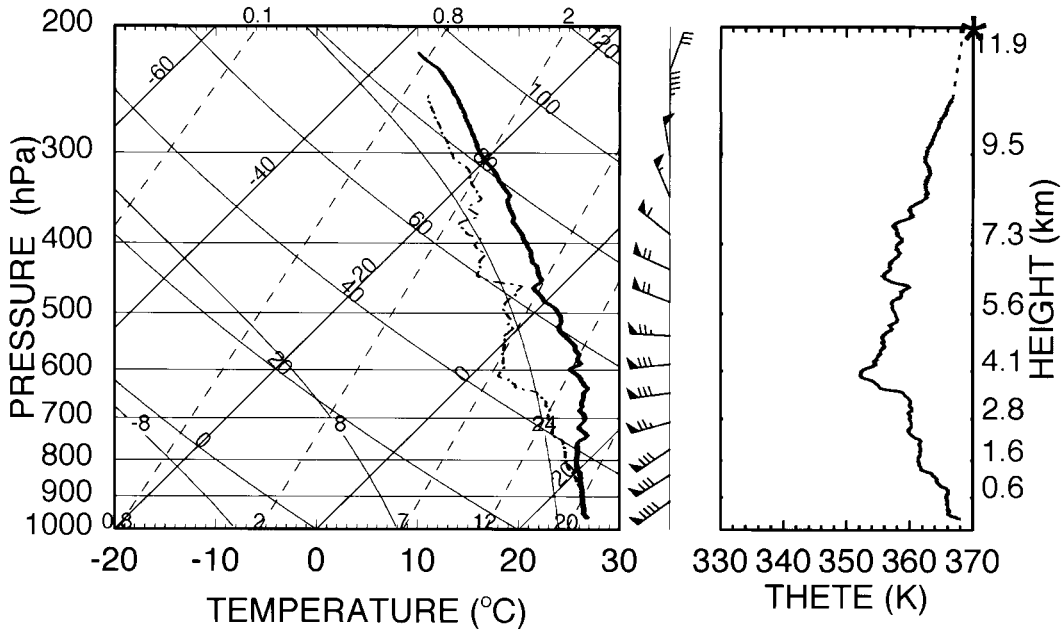
4. Finescale structure of the convective burst in EDOP observations

a. Hot tower C with eye subsidence

Figure 6 presents an EDOP flight line from 1950 to 2017, which cuts across the southern edge of cell C

(Fig. 3d) and typifies the finescale structure of Bonnie’s inner core. The upper panel provides attenuation-corrected reflectivity, whereas the lower panel shows vertical velocities calculated as described in section 2. Traces from the DC-8 flight-level θ_E and w are superimposed on the panel and centered on the mean DC-8 altitude; wind barbs are plotted with the head exactly at the DC-8 altitude (flags on barbs are 25 m s^{-1}). The DC-8 time and location were within about 160 s and 1 km of the ER-2, respectively, for most of the line. NOAA-42 flight level data taken about 1.8 h later and within 20 km of

a. EYE/EYEWALL 8/23/1998 185933 UTC



b. EYE 8/23/1998 212655 UTC

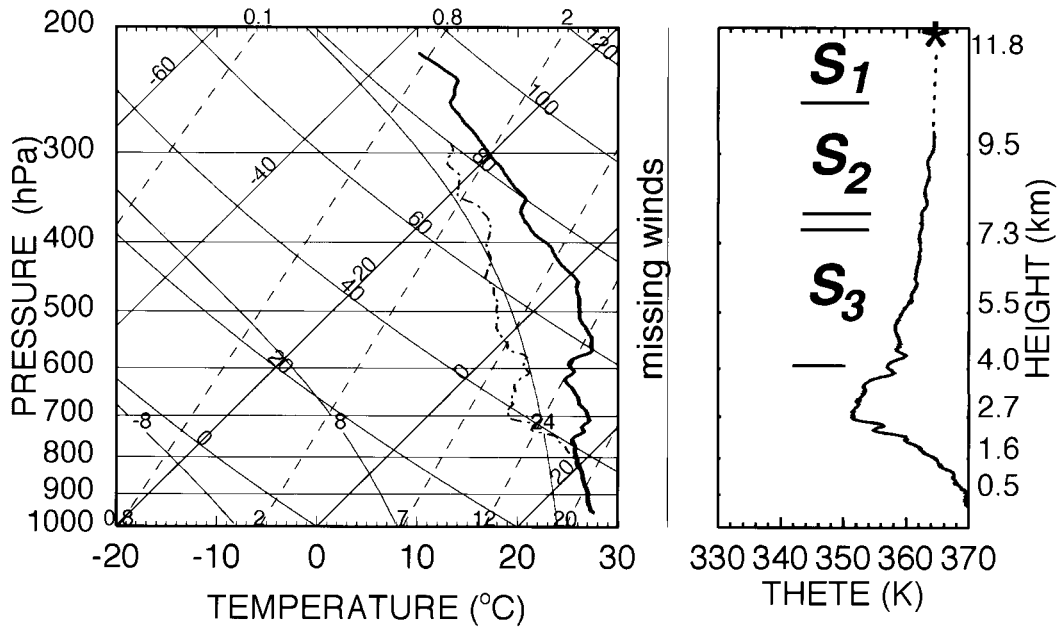
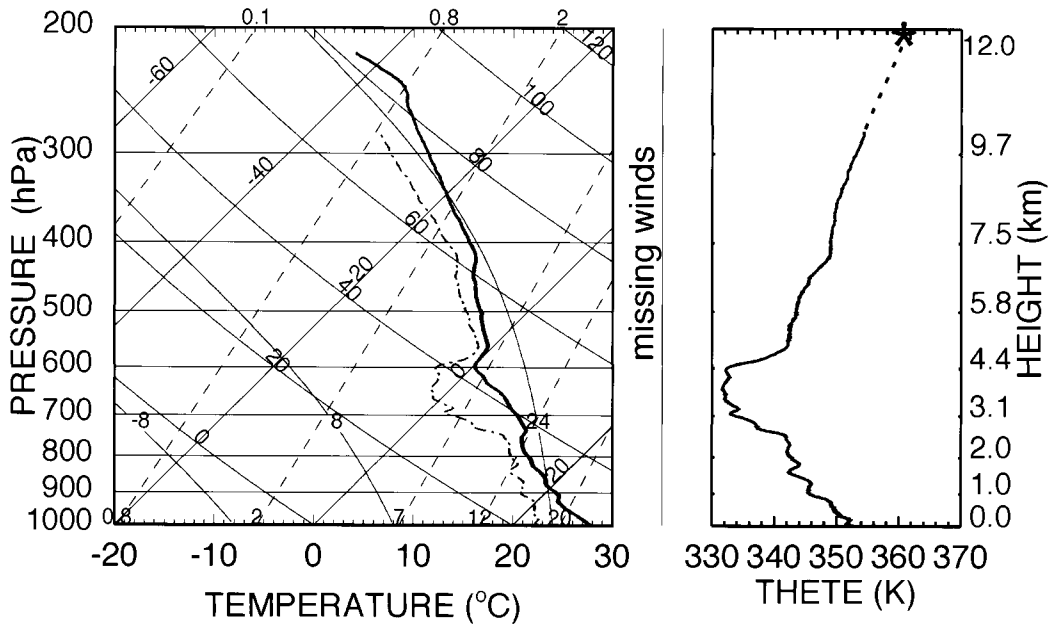


FIG. 5. Dropsonde releases in Hurricane Bonnie on 23 Aug 1998 at (a) 1859 in edge of south eyewall, (b) 2126 in eye center, (c) 1944 in the environment ~ 250 km east of the circulation center, and (d) 2040 in the northwest close-in environment. The location of the corresponding drop points are shown in Fig. 4. Left panel shows skew T plot. The right panel shows θ_E profile, where the "*" indicates the DC-8 flight-level value and the dashed portion of the curve is extrapolated between the top dropsonde level and the "*"; S_x , where $x = 1, 2,$ and 3 indicate subsidence layers. Wind barbs are pennant: 25 m s^{-1} , flag: 5 m s^{-1} , and half flag: 2.5 m s^{-1} .

c. ENVIRONMENT 8/23/1998 194401 UTC



d. ENVIRONMENT 8/23/1998 204042 UTC

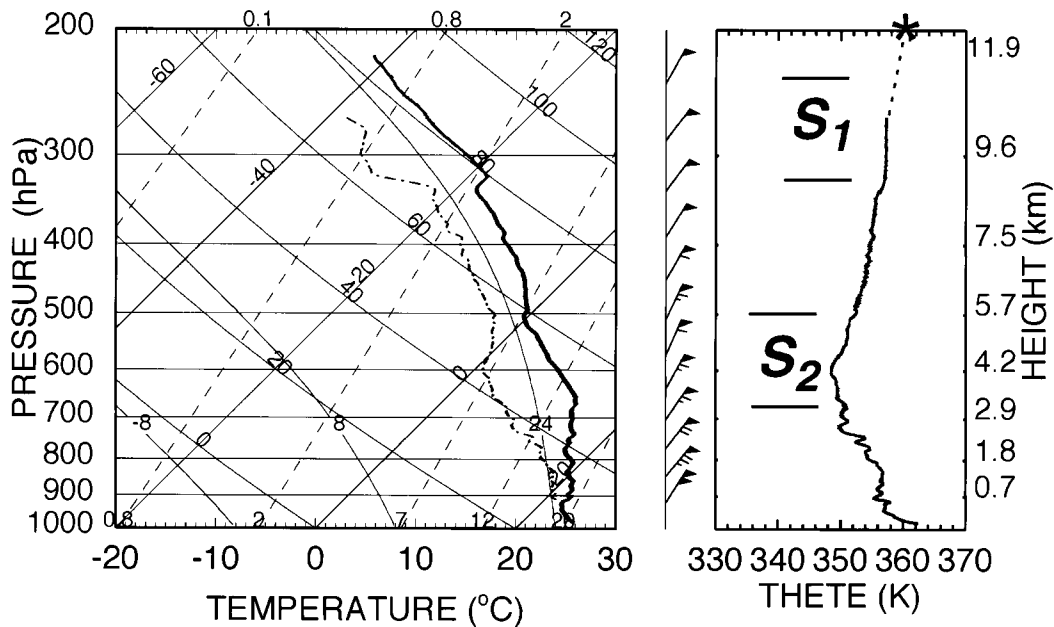


FIG. 5. (Continued)

the ER-2 and DC-8 flight lines are also superimposed, giving a lower-level view.

Similar to the radar composite (Fig. 4b), the eastern eyewall is very active, with peak reflectivities greater than 50 dBZ (Fig. 6, $x \sim 230$ km, where x corresponds to distance axis) extending from the surface to about 7-km altitude, with vertical velocities exceeding 6–8 m s^{-1} (red and white colors in Fig. 6). These are typical

magnitudes found in the updrafts of hurricane eyewalls (Black et al. 1996). The reflectivities were attenuated approximately 8 dBZ, and they were therefore corrected for attenuation as described in section 2a. The peak height of the eyewall updraft is approximately 16.5 km. There is also significant stratiform rain farther to the east and evidence of an outer eyewall ($x \sim 300$ km). The western eyewall ($x \sim 170$ – 180 km) is extremely

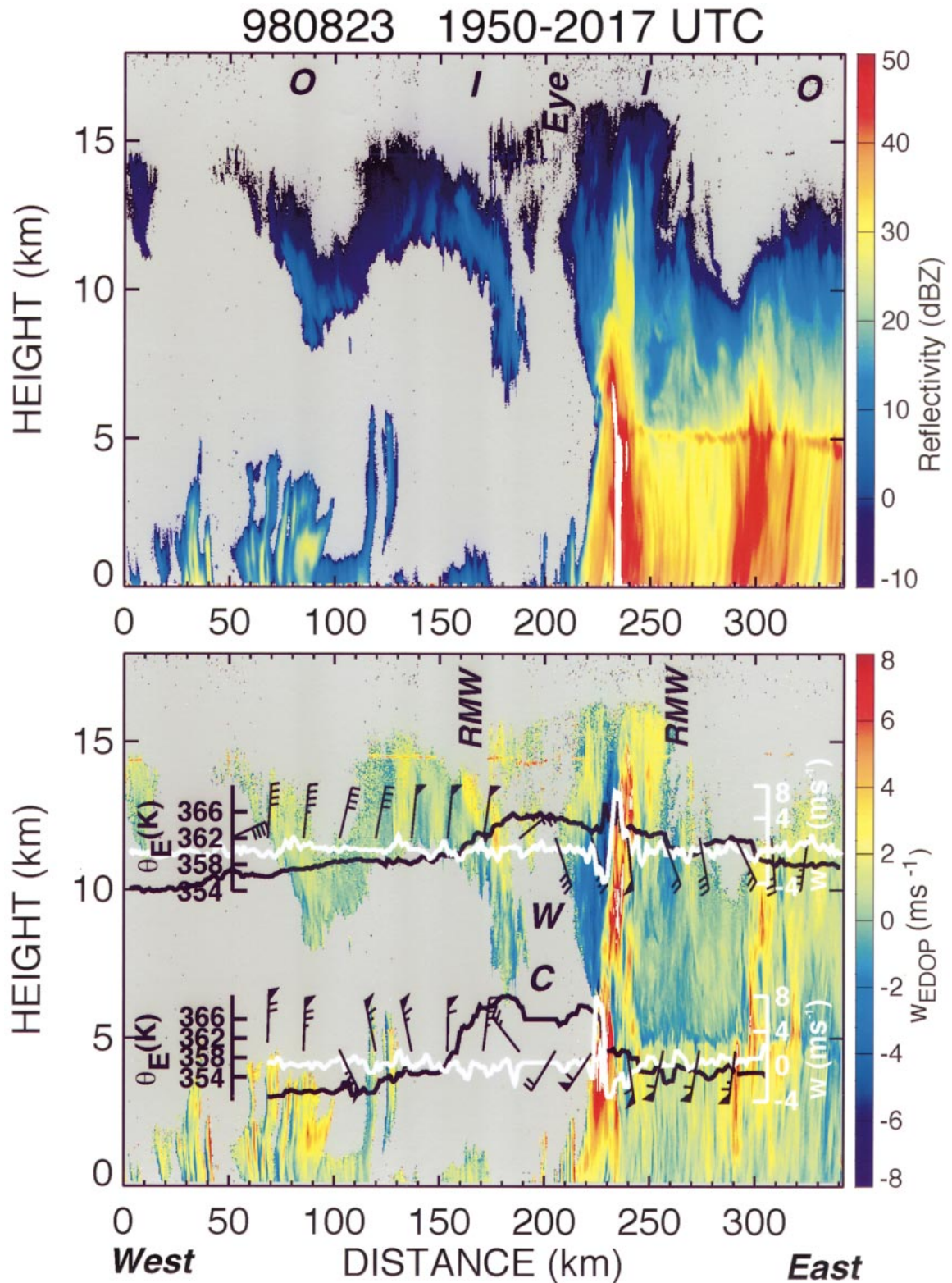


FIG. 6. EDOP reflectivity and vertical velocities w during 1950–2010 flight line. Traces show w (white) and θ_E (black) derived from the DC-8 flight-level data. Labels are shown for outer eyewall (O), inner eyewall (I), warm core (W), circulation center (C), and radius of maximum wind (RMW). Reflectivities (w) exceeding 50 dBZ (8 m s^{-1}) are white, and w less than -8 m s^{-1} are black. Wind barbs are pennant: 25 m s^{-1} , flag: 5 m s^{-1} , and half flag: 2.5 m s^{-1} . See text for details.

weak at upper levels and not detected by EDOP at lower levels. EDOP is observing mainly cirrus outflow to the west, also supported by the other flight lines (not shown) and the 2040 dropsonde (Fig. 5d), with subsidence beneath this cirrus layer whose base ranges up to 12-km altitude. Wind barbs from both aircraft clearly show the circulation center ($x \sim 200$ km), with maximum winds of 30 m s^{-1} at the WP-3D altitude and 25 m s^{-1} at the DC-8 altitude. The warm core is apparent in the θ_E traces with a 10-K warming from the DC-8 (~ 12 -km altitude), and 14-K warming from the WP-3D (~ 4.5 -km altitude). The corresponding temperature trace (not shown) has a warm core of 8°C for the DC-8 and 13°C for the WP-3D. Two days later, on 25 August, the AMSU on NOAA-15 obtained a profile of Bonnie's warm core (Kidder et al. 2000). The intensity of the storm was only slightly greater than on 23 August, so that a comparison of aircraft-measured temperatures to those from AMSU is useful. At the DC-8 level of 11.8 km ($\sim 39\,000$ ft), the temperature excess is in good agreement with the AMSU, whereas the lower WP-3D aircraft had values about 3 times (13° vs 4°C) that sensed by AMSU on 25 August. Part of this difference may be due to the spatial resolution of AMSU relative to the eye diameter and the associated beam-filling issues.

Figure 7 provides a zoomed image of Fig. 6, which emphasizes the structure of the eastern eyewall and the associated eyewall convection and strong subsidence within this portion of the eye. The edge of the eyewall is defined in the figure by the 5-dBZ reflectivity contour, and this contains a major portion of the eyewall updraft. The eyewall has strong EDOP-derived vertical velocities w (denoted w_{EDOP}) that exceed 10 m s^{-1} from 3-km up to 15-km altitude and high reflectivities, exceeding 50 dBZ, extending from the eyewall at 7-km altitude to its base. The w_{EDOP} are consistent with the in situ measurements from the DC-8 and WP-3D (Fig. 7, bottom), which show similar magnitudes of 8 – 10 m s^{-1} . The intensity of the updrafts plus high reflectivities suggest large rimed hydrometeors such as graupel or small hail falling out of the eyewall from above the freezing level at ~ 5.3 -km altitude. The strong downdraft at 7-km altitude near the origin of this reflectivity core is likely due to inadequately correcting for fall speeds. That is, a snow fall speed is assumed whereas the high w_{EDOP} are more likely due to higher-fall speed ice particles such as dense graupel or small hail.

The pronounced mesoscale subsidence in Fig. 7 (blue colors) covers a broad 25-km-wide region within Bonnie's eye ($x \sim 210$ – 235 km) and extends from near cloud-top level (15 km) down to about 6-km altitude. This feature is much deeper and more extensive than the compensatory downdrafts that commonly flank upper-level convective updrafts (Houze 1993). This subsidence region is independently confirmed by comparison of w_{EDOP} with the DC-8 in situ measurements (Fig. 8). Figure 8 was constructed by matching the EDOP measurement closest to the DC-8 flight-level measure-

ment, both spatially and in altitude. If the separation between the EDOP column and the DC-8 was greater than 4 km, the points were rejected; points are not shown for EDOP when the reflectivity is low in the absence of scatterers. The fall speeds with a maximum in the eyewall were calculated based on the fall speed–reflectivity relation and were adjusted for altitude (section 2a); fall speeds are reported as positive downward in Fig. 8.

Figure 8 shows that the eyewall updraft and subsidence within the eye observed by EDOP are confirmed by the independent in situ DC-8 measurements. One main reflectivity core exists in the updraft, with peak reflectivities of about 28 dBZ and maximum w_{EDOP} of about 8 m s^{-1} both from EDOP and the DC-8 MMS. The θ_E traces indicate values of 364–365 K within the updraft, increasing across the subsidence region to 368 K within the eye. The mixing ratio remains nearly constant across the updraft (0.35 g kg^{-1}) and then increases steadily to larger values in the eye.

The w curves for the DC-8 (w_{MMS}) and w_{EDOP} are similar but with some important differences. These differences, given by $w_{\text{MMS}} - w_{\text{EDOP}}$ in Fig. 8b, can arise from any of the following sources: (i) fall speed estimates used for correcting EDOP, (ii) errors in the w_{MMS} estimates, (iii) spatial and temporal displacements of the DC-8 and ER-2 measurements in strong gradients regions of w , and (iv) strong tangential air motions, which can bias the EDOP measurements. Significant differences in $w_{\text{MMS}} - w_{\text{EDOP}}$ occur in the transition between the updraft and downdraft regions ($x \sim 228$ – 232 km), where w_{EDOP} is lower than w_{MMS} ; this produces a $w_{\text{MMS}} - w_{\text{EDOP}}$ of about $+7.5 \text{ m s}^{-1}$. This large positive difference is likely due to improper fall speed removal, given that the ER-2 and DC-8 spatial and temporal differences are small (<0.5 km and <2 min), and the rotational winds (Fig. 8e) are not sufficiently large to cause a bias in the vertical velocities. It has been shown in Heymsfield (1988) that a strong cross-track wind (i.e., tangential wind) will produce an uncorrectable bias in the Doppler measurements when the roll angle is non-zero. The fall speed estimates in this transition resulting from the empirical snow reflectivity–fall speed relation had peak values of 2.4 m s^{-1} (Fig. 8b), whereas the DC-8 microphysics measurements suggested much larger fall speeds. Within this localized updraft–downdraft transition region, the DC-8 microphysics data indicated the presence of 2–3-mm heavily rimed spherical ice particles that could be classified as graupel or as frozen raindrops (A. Heymsfield and R. Black 2000, personal communication). The fall speeds of these large particles are likely to be significantly larger than given by the assumed snow reflectivity–fall speed relation, thereby producing an underestimate of w_{EDOP} . On the other hand, $w_{\text{MMS}} - w_{\text{EDOP}}$ in the updraft region ($x \sim 232$ – 238 km), which has higher reflectivities than the transition region, is about -3 to -4 m s^{-1} . This difference is unlikely to be associated with fall speed issues, but rather it may

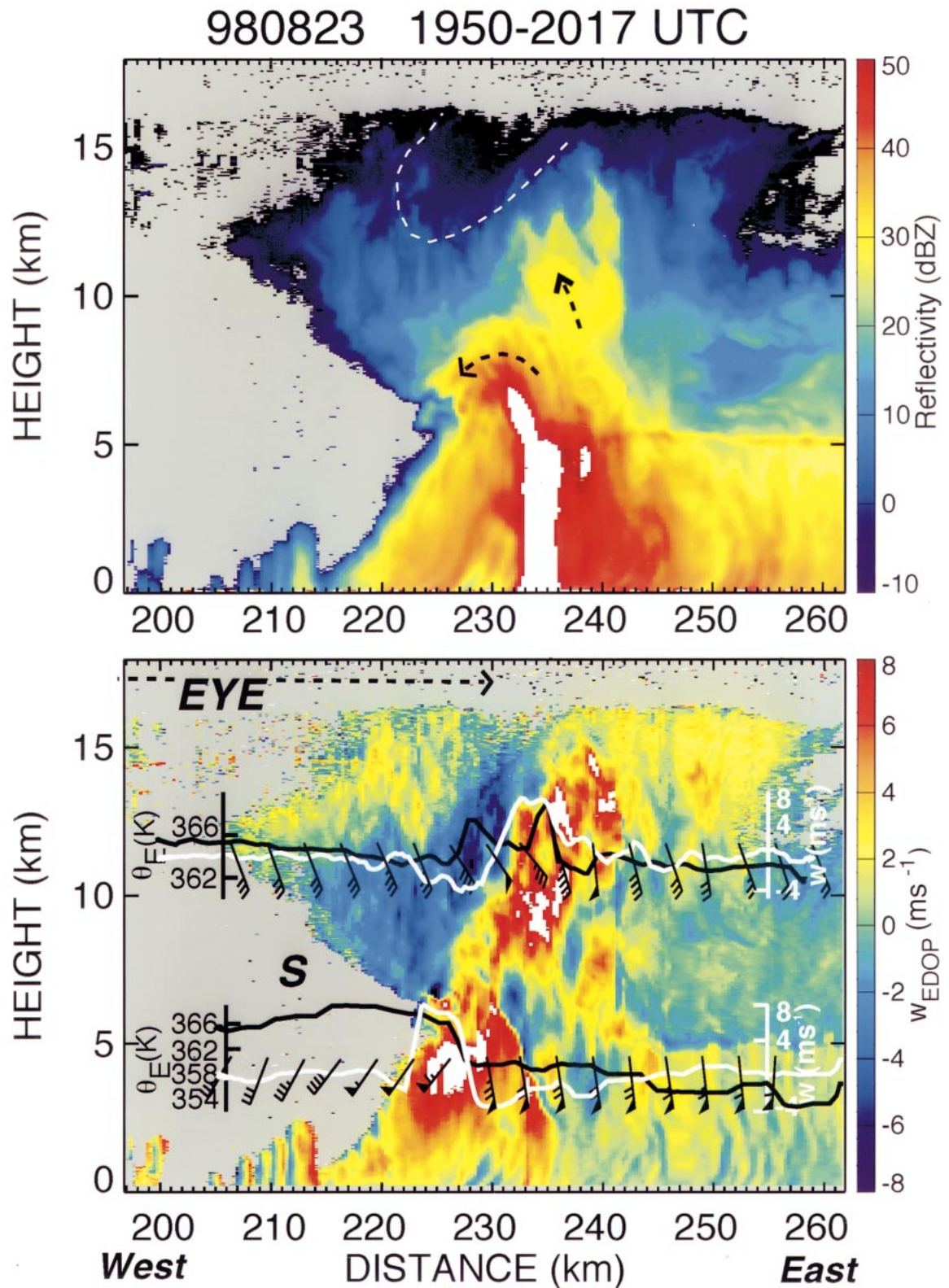


FIG. 7. Zoom of Fig. 6 indicating eyewall subsidence. The dashed line in the reflectivity plot shows an intruding region of low reflectivity at cloud top. Arrows indicate suggested detrainment of mass from eyewall updraft. The "S" indicates the subsidence region within the eye. Wind barbs are pennant: 25 m s^{-1} , flag: 5 m s^{-1} , and half flag: 2.5 m s^{-1} . See text for details.

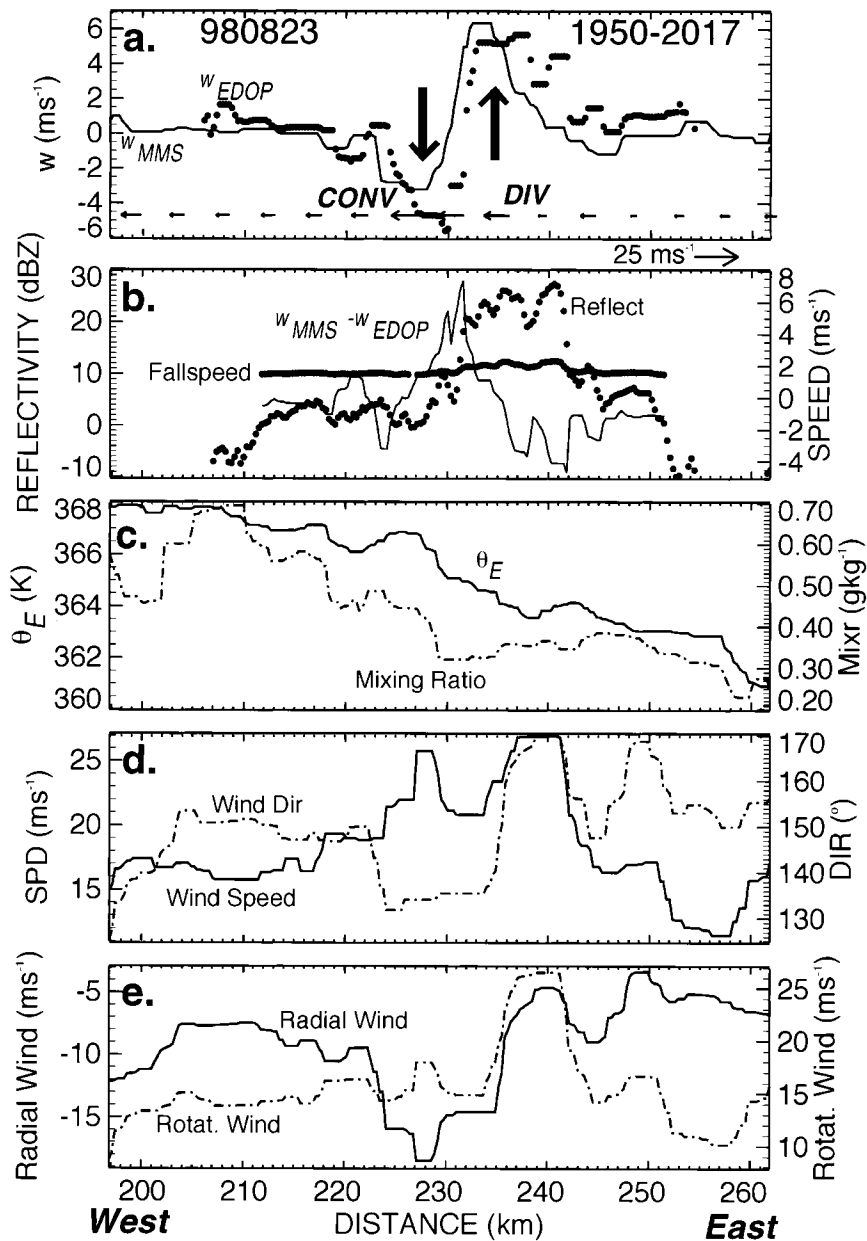


FIG. 8. Comparison of DC-8 flight line during 1950–2017: (a) EDOP-derived w (w_{EDOP}) and DC-8 flight-level w (w_{MMS}); (b) reflectivity, reflectivity-derived fall speed (positive downward), and the difference $w_{MMS} - w_{EDOP}$; (c) DC-8 flight-level θ_E and mixing ratio; (d) DC-8 flight-level wind speed and direction; (e) DC-8 flight-level rotational and radial wind. See text for details.

be attributed to biases in the Doppler velocities caused by the strong hurricane rotational wind component (Fig. 8e, $x \sim 236$ – 242 km) as mentioned above. The EDOP nadir antenna is never precisely at nadir, and although aircraft motions can be effectively removed, horizontal air motions cannot.

In view of the above, there are several important factors suggesting detrainment from the eyewall updraft into the subsidence region. First, the radial wind component shown by vectors in Fig. 8a and by the trace in

Fig. 8e show strong flow across the updraft–downdraft couplet. Speed divergence between the updraft and downdraft and speed convergence west of the downdraft suggest that the downdraft is *entraining* air out of the updraft, as first postulated by Malkus (1958). The outflow of updraft air into downdraft also causes the MMS winds to back about 20° while passing across the draft transition (Fig. 8d, $x \sim 235$ km). Furthermore, there is an approximately 5 m s^{-1} reduction of wind speed across the downdraft (Fig. 8d, $x \sim 230$ – 233 km), suggesting

downward transport of smaller momentum values from high levels.

b. Structure of overshooting hot tower D

Figure 9 covers a second vigorous overshooting hot tower illustrated in the satellite IR temperatures (cell D in Fig. 3a) and Fig. 4c. Figure 10 shows an enlargement of just this tower. This tower is northeast of the circulation center, and the radar cloud top extends up to 17.5-km altitude with an apparent 1.5–2-km “overshooting” region based on the Puerto Rico soundings. Similar to the previous flight line, the eyewall of the northeast and northwest quadrants of the circulation center is dominated by strong convection, with reflectivities exceeding 50 dBZ at low levels, whereas the eyewall structure southwest of the circulation center is weak in this respect. Furthermore, the cloud-top height is below 15 km on the west side of the storm as compared with the higher tops in the more convective region. The winds at the DC-8 altitude are strongest (25 m s^{-1}) in the western eyewall. At the lower WP-3D altitudes, peak winds are about 40 m s^{-1} . A strong warm core is present in the temperature fields (not shown) and also is apparent in θ_E values 8–10 K warmer than the environment (lower panel in Fig. 9) at the DC-8 altitude and an approximately 6-K warm core at WP-3D altitudes except within the eyewall, where θ_E is 368 K. A dropsonde was released at 2126 in the eye (Fig. 5b and located in Fig. 9) and indicates a deep warm core with θ_E of approximately 366 K at 12-km altitude extending down to θ_E of approximately 360 K at 5-km altitude. This is corroborated by θ_E from the WP-3D (Fig. 9), which is also approximately 360 K near 5-km altitude. Three pronounced subsidence layers labeled S_1 – S_3 can be inferred in Fig. 5b.

The vertical motion structure in hot tower D (Fig. 10) is complex at higher altitudes, with residual updrafts from the decaying tower and a dominance of downward motions between 5- to 10-km altitude. Similar to Fig. 8, Fig. 11 shows a comparison of the EDOP-derived vertical velocity and the DC-8 in situ measurements. Reflectivities aloft are lower than the previous flight line (Fig. 8b), with mainly one high-reflectivity core of 20 dBZ at $x \sim 240 \text{ km}$. The w_{EDOP} has two unspectacular updraft peaks of $\sim 4 \text{ m s}^{-1}$ at $x \sim 250 \text{ km}$ and 2 m s^{-1} at $x \sim 242 \text{ km}$ and a strong downdraft peak of -6 m s^{-1} at $x \sim 98 \text{ km}$. The w_{MMS} has one pronounced updraft at $x \sim 249 \text{ km}$ and near-zero vertical velocities from $x \sim 236$ to 242 km . As in Fig. 8b, the $w_{\text{MMS}} - w_{\text{EDOP}}$ has large positive values ($x \sim 239 \text{ km}$ and $x \sim 248 \text{ km}$). The images from the DC-8 in situ microphysics probes again showed larger graupel or frozen raindrops in this region as in section 3a. It is further surmised that this hot tower, having an overshoot of 1.5–2 km, is entering a dissipating stage with weakening updrafts and with large rimed hydrometeors lofted to high altitudes above the DC-8 level, now falling to lower levels. An over-

shoot of this amount theoretically would give a peak updraft speed of 30 m s^{-1} , which is of sufficient magnitude to sustain production of large rimed ice particles.² Cell-D cloud top is about 1 km higher than the eyewall convection cell C’s (Fig. 7) and would therefore support ice hydrometeors with larger fall speeds.

5. Discussion

Figure 12 presents a conceptual summary of the deduced relation between the convective burst, hot towers, and warm core in Hurricane Bonnie. The observations of hot towers presented indicate a large-magnitude (3 – 5 m s^{-1}) downdraft with deep penetration and surprisingly broad horizontal spread inside the eye of Hurricane Bonnie. The mechanism for the subsidence along the inner edge of the eyewall is hinted at by mainly circumstantial evidence, but the information taken together provides a coherent picture. There is indirect evidence for entrainment of drier stratospheric air at the tropopause within the overshooting convective tower. The top of the deep downdraft originates near the tropopause height (15-km altitude near $x \sim 230 \text{ km}$ in Fig. 7) and is adjacent to the convective tower updraft. A reflectivity notch is noted in the top of this hot tower near the origin of the subsidence (arrow in Fig. 7), and the reflectivity values are diminished within the upper 2–3 km of the hot tower (dashed line in Fig. 7). In addition, the strongly curved, deflected reflectivity features in Fig. 7a ($x \sim 230 \text{ km}$, 7-km altitude) all consistently point in direction from the updraft toward the subsidence region, suggesting that the downdraft is strong enough to entrain air from the updraft, as found in less spectacular tropical clouds by Malkus (1955). These features are also consistent with changes in wind speed and direction across the updraft–downdraft interface discussed earlier in section 4a. The above observations taken together suggest that compensating subsidence of dry stratospheric air is initiated by stratospheric overshoot of the tallest hot towers. Portions of the subsidence may be sustained by entrainment into the eye of moist cloudy air from the updraft, supplying liquid and/or ice hydrometeors to vaporize and to maintain the density of the descending current. Sublimation of the ice hydrometeors then cools the descending air and maintains the subsidence. Evidence presented by Malkus (1958) and Simpson et al. (1998) strongly suggests that dry adiabatic descent contributes to further eye warming after the hydrometeors have been fully vaporized. Other factors such as vertical pressure gradient forces also cannot be ruled out.

There is no obvious explanation why the second overshooting hot tower sampled (Fig. 10) did not show subsidence within the eye but instead produced localized

² Based on the laboratory work of Malkus (1960), which determined that a vertical velocity of 20 m s^{-1} is needed for every 1 km of overshoot into the stratospheric air.

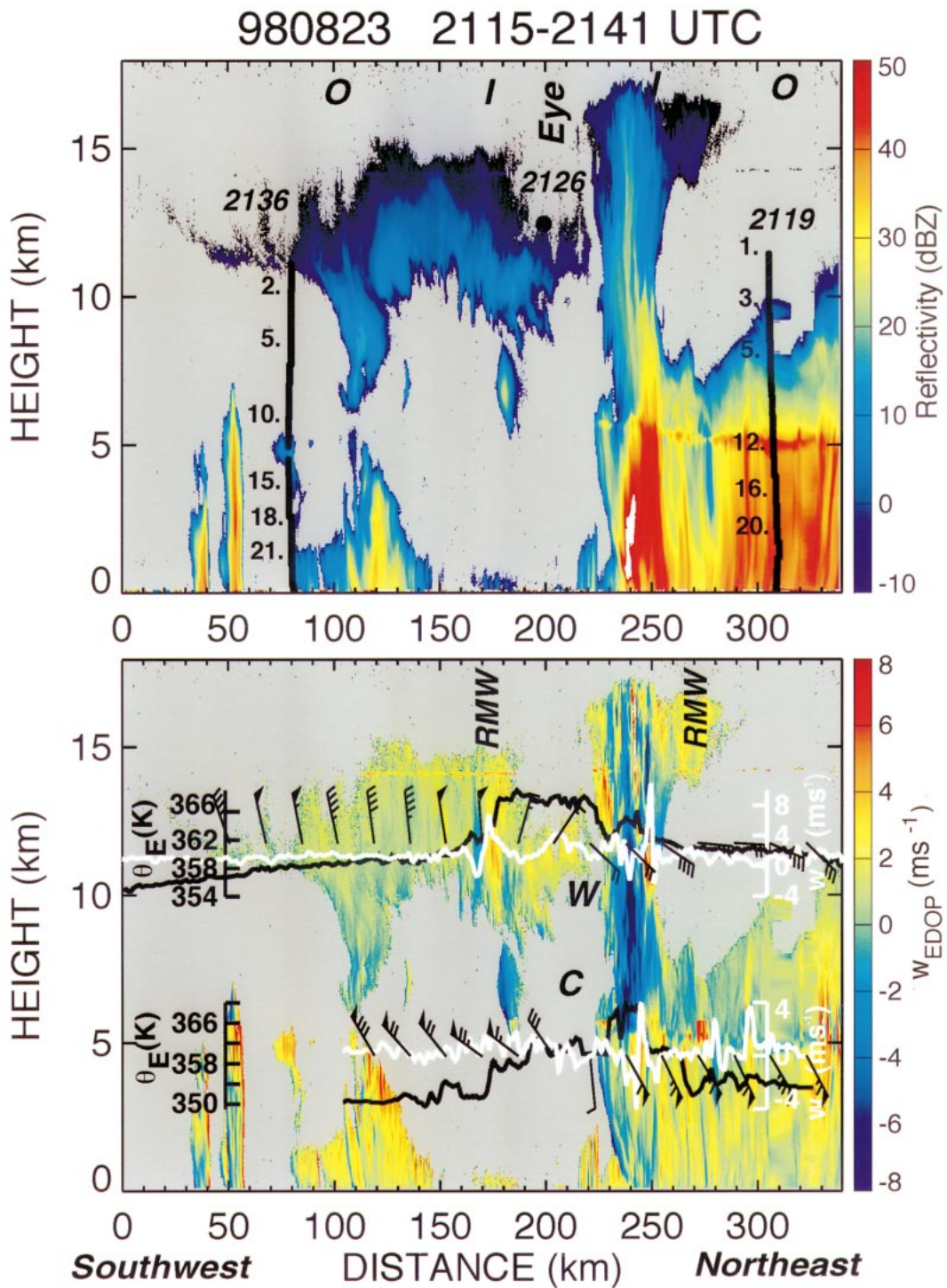


FIG. 9. Similar to Fig. 6, but for 2115–2134 flight line. Locations of dropsonde start time and fall trajectory are shown; numbers next to trajectory indicate distance in kilometers into (>0) or out of (<0) the plane of the cross section.

downdrafts *within* the cell at upper levels. This suggests that if subsidence related to deep convection does indeed play a role in eye warming, it may be sporadic in nature. Quite possibly not all vigorous overshooting hot towers

will produce eye interior subsidence. It is also possible that other occurrences of subsidence were entirely missed because of the sampling constraints of the aircraft mission; that is, not all hot towers in the convective

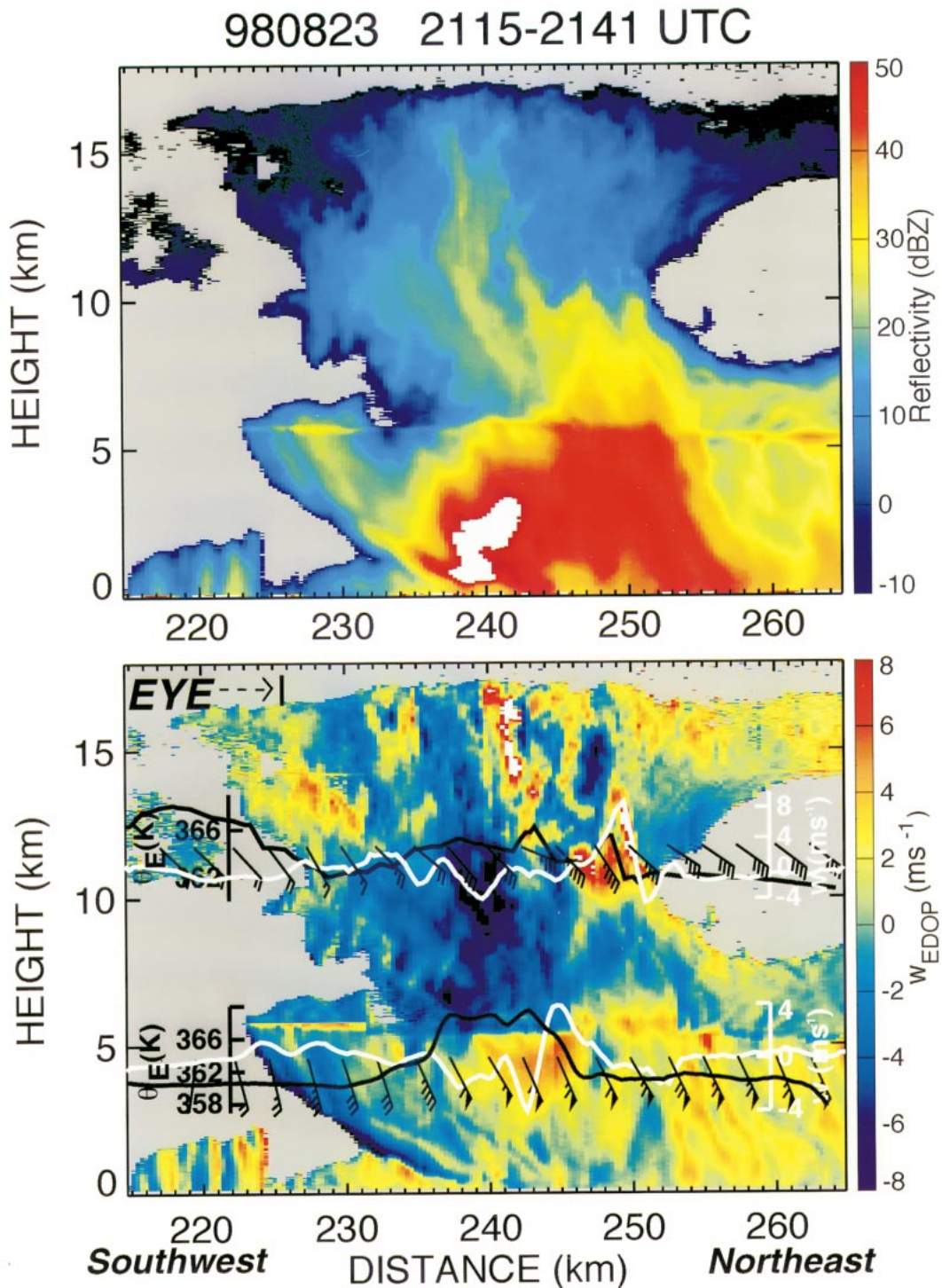


FIG. 10. Zoom of convective burst in 2115–2141 ER-2 flight line (similar to Fig. 7).

burst were flown, and those that were overflow (cells C and D) appeared to be in different stages of the life cycle. Nevertheless, the aggregate effect of numerous hot towers within a convective burst, a subset of which produces localized areas of deep subsidence inside the

eye, could engender inner-core warming on timescales characteristically longer than the convection itself, that is, over the duration of multiple vortex rotation periods.

The magnitude of eye warming resulting from subsidence in Bonnie is difficult to assess. There were two

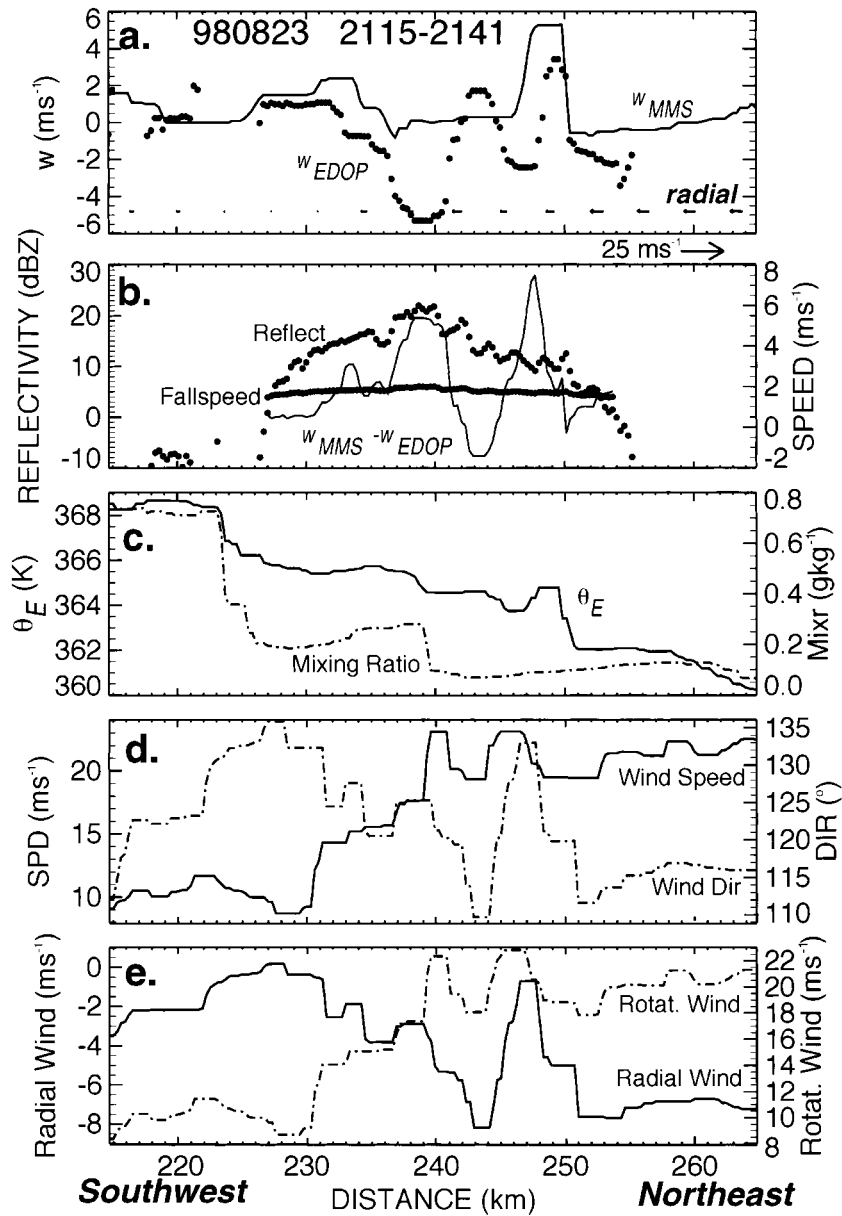


FIG. 11. Similar to Fig. 8, but for 2115–2141 flight line.

dropsondes made in the inner-core region of Bonnie—one at 1859 UTC, the other at 2126 UTC (Figs. 5a and 5b, respectively). The interval between these two drops encompasses the active period of cell C and its deep subsidence current. The 1859 UTC drop was made near the southern edge of the eye. Because of the largely moist neutral temperature profile and pronounced wind shear, it likely initially sampled air aloft within the eye, then spiraled down into the inner edge of the eyewall. It is hereinafter referred to as the “eyewall drop.” The second drop was initiated closer to the vortex center; although wind data are missing for this release, it more likely sampled the true eye environment during most if

not all of its descent. Accordingly, we refer to this second sounding as the “eye drop.”

When comparing the temperature profile between these two dropsondes, we note that the eye drop is uniformly warmer over a deep layer spanning the middle troposphere, extending from 430 hPa (~7 km) down to 640 hPa (~4 km). The maximum temperature difference is +3°C at 600 hPa (4 km). Other regions of the eye dropsonde are cooler relative to the eyewall drop, that is, a shallow layer below 640 hPa and at all levels above 370 hPa. Sharpening of the temperature profile at 2126 UTC into a pronounced inversion near 600 hPa is a signature of subsidence. Portions of the inversion tem-

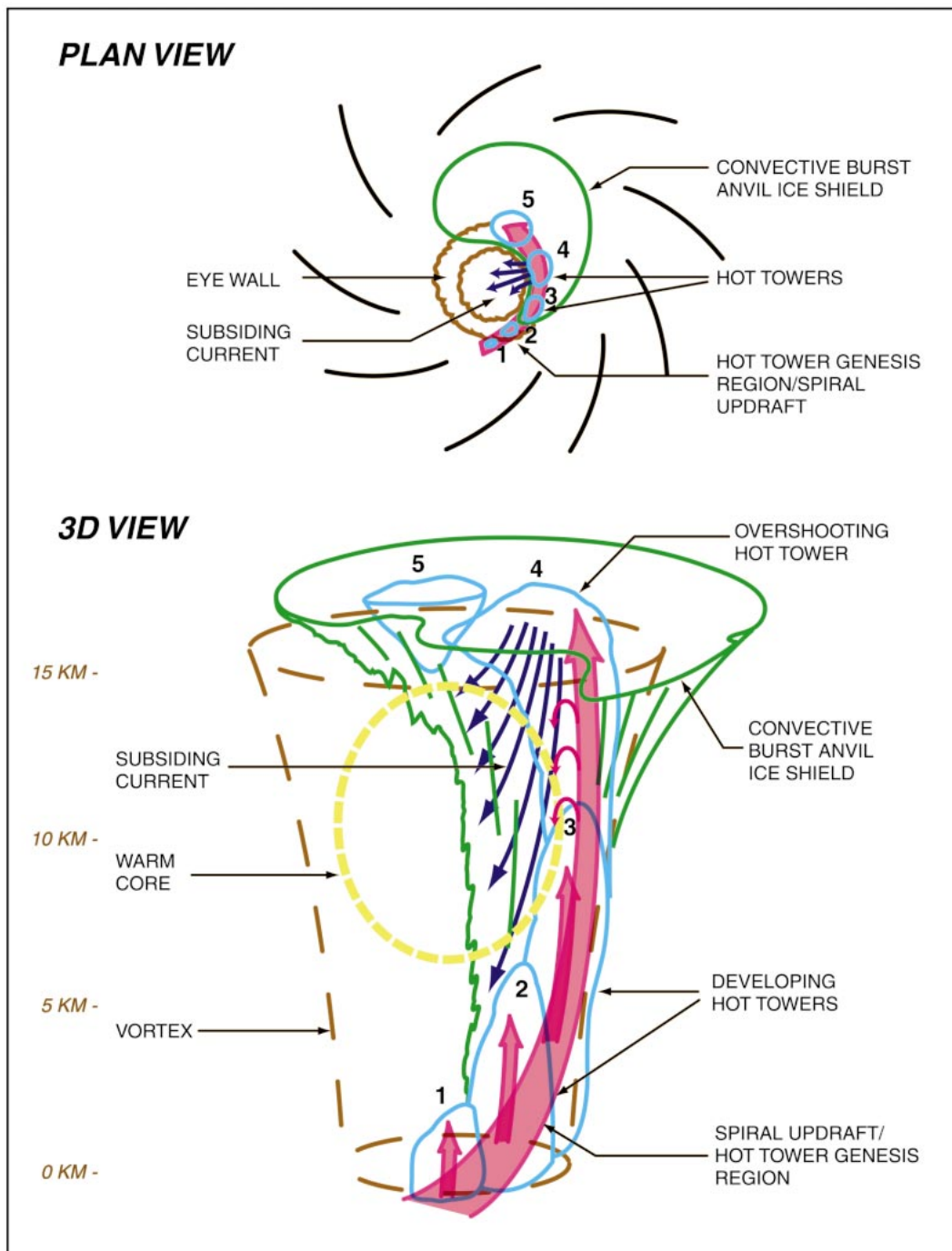


FIG. 12. Conceptual summary of Bonnie structure on 23 Aug 1998 derived from aircraft and satellite observations.

perature profile below 430 hPa are observed to approximate both dry adiabatic and moist adiabatic lapse rates. It is possible that the observed eye warming relative to the eyewall is correlated with the deep downdraft produced by cell C. We note that the eye drop is located downwind of cell C (2000 UTC), where counterclockwise spiral trajectories within the eye might have translated eye air modified by the deep downdraft. We also

cannot rule out the possibility that some of the observed differences in the temperature profiles between these two dropsondes are due to radial gradients in the warm-core temperature structure.

If an association between the deep subsidence and eye warming can be made, then the base of the observed subsidence inversion (4 km) would be located in the hydrometeor-free region of the subsiding air current

(Fig. 7, bottom panel)—were the current to extend below 5 km. The deep current possibly extends below this level where rapid melting and evaporation of hydrometeors render them undetectable to EDOP. Furthermore, deep cooling above the midlevel inversion (relative to the eyewall profile) is consistent with sublimation of hydrometeors in the upper reaches of the sinking current, offsetting adiabatic warming there. Only near the terminal end of the subsidence current does adiabatic warming dominate, as solid and liquid hydrometeors undergo nearly complete transformation to vapor.

The implications here, although not definitive, point to a possible contribution of deep convection-induced sinking motions from one or more hot towers to increases in the eye warm anomaly on the order of several degrees Celsius. This contribution is in addition to warming hypothesized to result from latent heat release within the eyewall hot towers that is manifested in the eyewall dropsonde temperature profile.

6. Conclusions

This paper has documented the finescale internal structure of a convective burst episode within Hurricane Bonnie during the end of its intensification and the relation of this burst to the warm core, using a synthesis of high-resolution datasets including GOES, EDOP aircraft radar, and in situ data. The multi-aircraft flight lines over Bonnie have provided unique measurements of the vertical precipitation and thermodynamic structure at higher altitudes than previously obtainable. Two hot towers within the convective burst were presented that differed in several respects, possibly because of the evolution of the hot towers and their relatively short lifetimes (less than 0.5 h). A key finding is the observation of a broad current of subsiding air within the eye during one of the hot-tower flight lines, originating at tropopause height. The second intense hot tower with cloud tops of 17.5 km was in a dissipating state and contained mainly downdrafts *within* the tower rather than in the eye. There is evidence that up to 3°C of warming between 5 and 6 km relative to the eyewall may result from deep descent from tropopause height. If the warming in the eye is the result of convection-induced subsidence, then this process may be sporadic and episodic rather than uniform, weaker subsidence operating throughout the entire eye. Only circumstantial evidence can be provided for the causes of the subsidence associated with the hot towers. This involves a combination of air detraining from the eyewall updraft and stratospheric air subsiding along the inner edge of the eyewall updraft, as postulated by Malkus (1958). She was intrigued by early radar evidence (Kessler 1957) showing the descent of eyewall cloud matter. This descent was shown to be essential by calculations from radiosonde eye and environment observations in a moderate and an intense tropical cyclone.

The Bonnie datasets analyzed here have provided a unique first look at finescale details of intense eyewall hot towers and their relationship to the warm core. Still, many unanswered questions remain. The frequency and distributions of hot towers and any associated subsidence regions are unknown. The relative contributions of the various subsidence-producing mechanisms also need to be addressed. Further analysis of the current datasets and planned future experiments such as CAMEX-4 should supply crucial evidence addressing these questions.

Acknowledgments. The CAMEX-3 analysis in this paper was supported by Dr. Ramesh Kakar at NASA Headquarters with TRMM funds and NASA-sponsored U.S. Weather Research Program efforts. There are a number of key people in field campaign operations that deserve special credit. Excellent coordination of the aircraft flights in Hurricane Bonnie was only possible through efforts of Dr. Ed Zipser, Ms. Robbie Hood, and NOAA Hurricane Research Division (Dr. Frank Marks and colleagues), combined with the excellent work of the ER-2 and DC-8 pilots. Dr. Robert Simpson provided valuable suggestions on the manuscript. Dr. Bart Geerts was extremely helpful in the data collection and initial analysis of Bonnie. Dr. Steve Bidwell and Mr. Ed Zenker are greatly appreciated for the superb engineering effort on the EDOP instrument. NOAA HRD (Dr. Frank Marks, Dr. Bob Black, and Mr. Paul Willis) provided WP-3D flight-level data and DC-8 microphysics information used in this analysis. Other datasets were obtained through the Marshall Space Flight Center CAMEX-3 archive. Many others answered the numerous questions that arose because of the diverse nature of the datasets used in this paper.

REFERENCES

- Black, M. L., R. W. Burpee, and F. D. Marks Jr., 1996: Vertical motion characteristics of tropical cyclones determined with airborne Doppler radial velocities. *J. Atmos. Sci.*, **53**, 1887–1909.
- Black, R. A., and J. Hallett, 1986: Observation of the distribution of ice in hurricanes. *J. Atmos. Sci.*, **43**, 802–822.
- Bolton, D., 1980: The computation of equivalent potential temperature. *Mon. Wea. Rev.*, **108**, 1046–1053.
- Chan, K. R., J. Dean-Day, S. W. Bowen, T. P. Bui, 1998: Turbulence measurements by the DC-8 meteorological measurement system. *Geophys. Res. Lett.*, **25**, 1355–1358.
- Danielsen, E. F., 1993: In situ evidence of rapid, vertical, irreversible transport of lower tropospheric air into the lower tropical stratosphere by convective cloud turrets and by large-scale upwelling in tropical cyclones. *J. Geophys. Res.*, **98**, 8665–8681.
- DeMaria, M., and J. Kaplan, 1999: An updated statistical hurricane intensity predictive scheme (SHIPS) for the Atlantic and eastern North Pacific basins. *Wea. Forecasting*, **14**, 326–337.
- Geerts, B., G. M. Heymsfield, L. Tian, J. B. Halverson, A. Guillory, and M. I. Mejia, 2000: Hurricane Georges's landfall in the Dominican Republic: Detailed airborne Doppler radar imagery. *Bull. Amer. Meteor. Soc.*, **81**, 999–1018.
- Gentry, R. C., T. T. Fujita, and R. C. Sheets, 1970: Aircraft, spacecraft, satellite and radar observations of Hurricane Gladys, 1968. *J. Appl. Meteor.*, **9**, 837–850.

- Gray, W., 1998: The formation of tropical cyclones. *Meteor. Atmos. Phys.*, **67**, 37–69.
- Hawkins, H. F., and D. T. Rubsame, 1968: Hurricane Hilda, 1964 II. Structure and budgets of the hurricane on October 1, 1964. *Mon. Wea. Rev.*, **96**, 617–636.
- Heysmsfield, G. M., 1989: Accuracy of vertical air motions from nadir-viewing Doppler airborne radars. *J. Atmos. Oceanic Technol.*, **6**, 1079–1082.
- , and Coauthors, 1996: The EDOP radar system on the high-altitude NASA ER-2 aircraft. *J. Atmos. Oceanic Technol.*, **13**, 795–809.
- , J. B. Halverson, and I. J. Caylor, 1999: A wintertime Gulf Coast squall line observed by EDOP airborne Doppler radar. *Mon. Wea. Rev.*, **127**, 2928–2949.
- Hock, T. F., and J. L. Franklin, 1999: The NCAR GPS dropwindsonde. *Bull. Amer. Meteor. Soc.*, **80**, 407–420.
- Holliday, C. R., and A. H. Thompson, 1979: Climatological characteristics of rapidly intensifying typhoons. *Mon. Wea. Rev.*, **107**, 1022–1034.
- Houze, R. A., Jr., 1993: *Cloud Dynamics*. Academic Press, 573 pp.
- Iguchi, T., and R. Meneghini, 1994: Intercomparison of single-frequency methods for retrieving a vertical rain profile from airborne or spaceborne radar data. *J. Atmos. Oceanic Technol.*, **11**, 1507–1516.
- Kessler, E., 1957: Eye region of Hurricane Edna, 1954. *J. Meteor.*, **15**, 264–270.
- Kidder, S. Q., W. M. Gray, and T. H. VonderHaar, 1978: Estimating tropical cyclone pressure and outer winds from satellite microwave data. *Mon. Wea. Rev.*, **106**, 1458–1464.
- , M. D. Goldberg, R. M. Zehr, M. DeMaria, J. F. W. Purdom, C. S. Veldon, N. C. Grody, and S. J. Kusselson, 2000: Satellite analysis of tropical cyclones using the Advanced Microwave Sounding Unit (AMSU). *Bull. Amer. Meteor. Soc.*, **81**, 1241–1259.
- Kuo, H.-L., 1959: Dynamics of convective vortices and eye formation. *The Atmosphere and Sea in Motion*, B. Bolin, Ed., Rockefeller Institute Press, 413–424.
- Lyons, W. A., and C. S. Keen, 1994: Observations of lightning in convective supercells within tropical storms and hurricanes. *Mon. Wea. Rev.*, **122**, 1897–1916.
- Malkus, J., 1955: On the formation and structure of downdrafts in cumulus clouds. *J. Meteor.*, **12**, 350–357.
- , 1958: On the structure and maintenance of the mature hurricane eye. *J. Meteor.*, **15**, 337–349.
- , and H. Riehl, 1960: On the dynamics and energy transformations in steady state hurricanes. *Tellus*, **12**, 1–20.
- Marks, F. D., and R. A. Houze Jr., 1987: Inner core structure of Hurricane Alicia from airborne Doppler radar observations. *J. Atmos. Sci.*, **44**, 1296–1317.
- , —, and J. F. Gamache, 1992: Dual-aircraft investigation of the inner core of Hurricane Norbert. Part I: Kinematic structure. *J. Atmos. Sci.*, **49**, 919–942.
- May, R. D., 1998: Open-path, near-infrared tunable diode laser spectrometer for atmospheric measurements of H₂O. *J. Geophys. Res.*, **103**, 19 161–19 172.
- Riehl, H., 1954: *Tropical Meteorology*. McGraw-Hill, 392 pp.
- Rodgers, E. B., W. S. Olson, V. M. Karyampudi, and H. F. Pierce, 1998: Satellite-derived latent heating distribution and environmental influences in Hurricane Opal (1995). *Mon. Wea. Rev.*, **126**, 1229–1247.
- Shapiro, L. J., and H. E. Willoughby, 1982: The response of balanced hurricanes to local sources of heat and momentum. *J. Atmos. Sci.*, **39**, 378–394.
- Simpson, J., J. B. Halverson, B. S. Ferrier, W. A. Petersen, R. H. Simpson, R. Blakeslee, and S. L. Durden, 1998: On the role of “hot towers” in tropical cyclone formation. *Meteor. Atmos. Phys.*, **67**, 15–35.
- Simpson, R. H., and J. Simpson, 1966: Why experiment on tropical hurricanes? *Trans. N.Y. Acad. Sci.*, **28**, 1045–1062.
- Smith, R. K., 1980: Tropical cyclone eye dynamics. *J. Atmos. Sci.*, **37**, 1227–1232.
- Steranka, J., E. B. Rodgers, and R. C. Gentry, 1986: The relationship between satellite measured convective bursts and tropical cyclone intensification. *Mon. Wea. Rev.*, **114**, 1539–1546.
- Stossmeister, G. J., and G. M. Barnes, 1992: The development of a second circulation center within Tropical Storm Isabel (1985). *Mon. Wea. Rev.*, **120**, 685–697.
- Veldon, C. S., and K. F. Brueske, 1999: Tropical cyclone warm cores as observed from the NOAA polar orbiting satellite’s new AMSU. Preprints, *23rd Conf. on Hurricanes and Tropical Meteorology*, Dallas, TX, Amer. Meteor. Soc., 182–184.
- , B. M. Goodman, and R. T. Merrill, 1991: Western North Pacific tropical cyclone intensity estimation from NOAA polar-orbiting satellite microwave data. *Mon. Wea. Rev.*, **119**, 159–168.
- Willoughby, H. E., 1998: Tropical cyclone eye thermodynamics. *Mon. Wea. Rev.*, **126**, 3053–3067.
- Zehr, R. M., 1992: Tropical cyclogenesis in the western North Pacific. NOAA Tech. Rep. NESDIS 61, 181 pp.
- Zhang, D.-L., Y. Liu, and M. K. Yau, 2000: A multiscale numerical study of Hurricane Andrew (1992). Part III: Dynamically induced vertical motion. *Mon. Wea. Rev.*, **128**, 3772–3788.